Journal of Magnetic Resonance 201 (2009) 199–204

Contents lists available at ScienceDirect

Journal of Magnetic Resonance

journal homepage: www.elsevier.com/locate/jmr

Cross-encoded magnetic resonance imaging in inhomogeneous fields

Raphael Paquin [a,b,*], Philippe Pelupessy [a,*], Geoffrey Bodenhausen [a,b]

[a] Département de Chimie, associé au CNRS, Ecole Normale Supérieure, 24 rue Lhomond, 75231 Paris Cedex 05, France
[b] Institut des Sciences et Ingénierie Chimiques, Ecole Polytechnique Fédérale de Lausanne, Batochime, 1015 Lausanne, Switzerland

ARTICLE INFO

Article history:
Received 29 July 2009
Revised 28 August 2009
Available online 11 September 2009

Keywords:
Magnetic resonance imaging (MRI)
Echo-planar imaging (EPI)
Inhomogeneous magnetic fields
Adiabatic radio-frequency pulses
Susceptibility effects
Slow motion

ABSTRACT

In magnetic resonance imaging (MRI), it is possible to cancel the effects of severe inhomogeneities of the magnetic field even if the field profile is unknown. The new 'cross-encoded' method is based on adiabatic frequency-modulated pulses combined with two orthogonal gradients that are applied simultaneously during encoding and decoding. Undistorted two- and three-dimensional images can be obtained in inhomogeneous fields where the breadth of the water resonance extends over several kHz.

1. Introduction

Magnetic resonance imaging (MRI) is undoubtedly the most popular application of nuclear magnetic resonance [1], with wide-ranging implications for medical diagnosis, neurosciences, metabolism, and material science. Although the objects or living organisms should ideally be immersed in a magnetic field that is as homogeneous as possible, it is often too difficult or costly to fulfill this stringent requirement. In living organisms, the quality of the images is degraded in the vicinity of voids and surgical implants. Inanimate objects may also suffer from discontinuities of the magnetic susceptibility. Temporal variations that occur in stimulated brains mapped by functional MRI [2,3] call for fast imaging techniques, such as echo planar imaging (EPI) introduced by Mansfield and co-workers [4]. Inspired by these experiments, Frydman and co-workers introduced single-scan methods for 'ultrafast' spectroscopy [5]. Recently, these ideas were extended to imaging [6], making it possible to probe 'real' Cartesian space directly without relying on Fourier transformation [7] or back-projection [1]. These methods were designed to cope with inhomogeneous fields with *known* profiles, where the encoding schemes can be tailored to compensate for the phase dispersion arising from the inhomogeneity of the static field [8]. In this work, we shall present *cross-encoded* single-scan methods that are designed to compensate for effects of inhomogeneous fields in a fraction of a second *without* requiring any knowledge of their spatial profiles.

2. Principles

2.1. Homogeneous fields

In Fig. 1, a selective pulse combined with a gradient G_y^s is applied along the y axis to excite the magnetization in a $\{x, z\}$ plane. In contrast to earlier methods for single-scan spectroscopy [9], orthogonal G_x^e encoding gradients of duration T_e must be combined with G_z^e encoding gradients. In the decoding interval, the G_z^d gradients unwind the phase accumulated during the G_x^e encoding gradients, instead of the chemical shifts in our earlier methods. We assume that only a single chemical shift $\Omega = 0$ is present. Thus the precession frequency of the magnetization associated with a voxel centered on the coordinates $\vec{r} = \{x, y, z\}$ during the first adiabatic pulse is

$$\omega_{\vec{r}} = \gamma \vec{G} \cdot \vec{r} = \gamma(G_x^e x + G_z^e z) \tag{1}$$

The sign of G_z^e is opposite during the second adiabatic pulse. The frequency sweep of the adiabatic pulse $-\Delta\omega_{ad}/2 \leqslant \omega_{RF} \leqslant \Delta\omega_{ad}/2$ is defined so that the center of the sweep corresponds to the Larmor frequency in the absence of any gradients. The phase at the end of the encoding block is:

$$\varphi_e(x, z) = -\lambda xz \tag{2}$$

where

* Corresponding authors.
E-mail addresses: raphael.paquin@ens.fr (R. Paquin), philippe.pelupessy@ens.fr (P. Pelupessy).

1090-7807/$ - see front matter © 2009 Elsevier Inc. All rights reserved.
doi:10.1016/j.jmr.2009.09.008

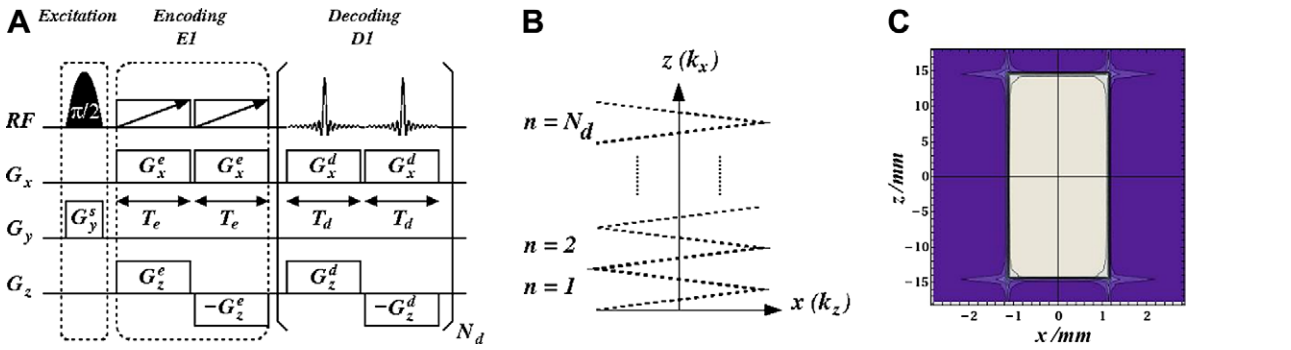

Fig. 1. Characteristics of cross-encoded magnetic resonance imaging (CE-MRI). (A) Excitation of transverse magnetization in a slice $\{x, z\}$ perpendicular to the y axis is achieved with a selective radio-frequency (*RF*) pulse in the presence of a field gradient G_y^s. The simplest encoding sequence $E1$ comprises two adiabatic *RF* pulses (rectangles with diagonal arrows) of duration T_e, applied in conjunction with a pair of opposite gradients G_z^e and a pair of identical gradients G_x^e. In the simplest case, decoding $D1$ is achieved by applying two identical gradients G_x^d and a pair of opposite gradients G_z^d, each of duration T_d. This scheme is repeated N_d times. (B) The Cartesian (real) $\{x, z\}$ space is probed directly through zig-zag trajectories imposed by the decoding sequence. (C) Numerical simulation of the image of a rectangular two-dimensional object of dimensions 2×30 mm, obtained with the pulse scheme (A). The absolute value of the integral of Eq. (4) has been calculated at intervals $\Delta x = x_{max}/100$ and $\Delta z = z_{max}/100$ for $-x_{max}/2 < x < x_{max}/2$ and $-z_{max}/2 < x < z_{max}/2$ with the following parameters $\gamma(^1H) = 2.6752$ rad/(T s), $G_x^e = G_z^e = G_x^d = 0.022$ T/m, $G_z^d = 0.22$ T/m, $T_e = 6$ ms, $T_d = 320$ μs, $\Delta\omega_{ad}/(2\pi) = 40$ kHz, $N_d = 32$, resulting in $x_{max} \sim 5.7$ mm and $z_{max} \sim 36.4$ mm.

$$\lambda = 4T_e\gamma^2 G_x^e G_z^e/\Delta\omega_{ad} \tag{3}$$

This equation is symmetric with respect to a permutation of the x and z coordinates. Thus, if the G_z^e gradient encodes for the x coordinate, the G_x^e gradient will do the same for the z coordinate. In contrast to traditional k-space MRI using Fourier transformations, the decoding sequence leads to a trajectory in the $\{x, z\}$ plane [8], which can be chosen at will. Fig. 1A shows a decoding scheme $D1$ based on the simultaneous application of gradients G_x^d and G_z^d of duration T_d. Pairs of such gradients, with alternating signs in the latter dimension, must be repeated N_d times. This procedure gives the 'zig-zag' trajectory illustrated in Fig. 1B [8]. The signal at time t is

$$S(t) = \int\int_{allx,z} A(x,z)exp[i\varphi_e(x,z)] \times exp[ik_x(t)x + ik_z(t)z]dxdz \tag{4}$$

where $A(x, z)$ is the amplitude of the initial longitudinal magnetization, and $k_x(t)$ and $k_z(t)$ are defined as

$$k_x(t) = \gamma\int_0^t G_x^d(t')dt' \quad k_z(t) = \gamma\int_0^t G_z^d(t')dt' \tag{5}$$

$$G_x^d(t') = G_x^d \quad G_z^d(t') = (-1)^{n_{D1}(t')}G_z^d \tag{6}$$

where $n_{D1}(t')$ is the integer part of the fraction t'/T_d, which toggles between +1 or −1 for positive and negative lobes of the train of bipolar decoding gradients.

As explained by Shrot and Frydman [6], the overall phase Φ should not vary across a voxel V_k centered on the coordinates (x_k, z_k)

$$\frac{\partial}{\partial x}[\Phi(x,z,t)]_{(x_k,z_k)} = 0 \quad \text{and} \quad \frac{\partial}{\partial z}[\Phi(x,z,t)]_{(x_k,z_k)} = 0 \tag{7}$$

with

$$\Phi(x,z,t) = \varphi_e(x,z) + k_x(t)x + k_z(t)z \tag{8}$$

From Eqs. (2), (7), and (8), the relation between the coordinates (x_k, z_k) of the voxel V_k and the variables $k_x(t)$ and $k_z(t)$ is:

$$x_k = \frac{k_z(t_k)}{\lambda} \quad \text{and} \quad z_k = \frac{k_x(t_k)}{\lambda} \tag{9}$$

Thus at time t_k in the decoding sequence, an echo signal appears that reveals the position (x_k, z_k) of the voxel V_k. The x dimension is decoded by the z gradient and vice versa. While the k_x "walk" occurs during $2N_dT_d$ due to the continuous application of G_x^d, the k_z trajectory is reversed every T_d when the sign of G_z^d changes.

In Fig. 1C, an image that could be obtained with the adiabatic pulse scheme of Fig. 1A is simulated for an ideal rectangular object. Only minor distortions are apparent around the edges of the object, in particular near the corners.

2.2. Inhomogeneous fields

In a static (time-independent) inhomogeneous field, the precession frequency of the magnetization of a voxel V_k in the encoding interval is $\omega_{\vec{r}} = \gamma\{G_x^e x + G_z^e z + \delta B_0(x,y,z)\}$. The additional term is due to the (unknown) spatial variation of the static field $B_0(x, y, z)$. The phase at the end of the simple encoding scheme $E1$ of Fig. 1 is:

$$\varphi_{E1}(x,z) = -\lambda_{E1}xz \tag{10}$$

where

$$\lambda_{E1} = 4T_e\gamma^2(G_x^e G_z^e + G_z^e\delta B_0(x,y,z)/x)/\Delta\omega_{ad} \tag{11}$$

Compensation of static inhomogeneities during encoding can be achieved by the scheme of Fig. 2. After the initial encoding sequence $E1$, a second sequence $E2$ is inserted, where the signs of

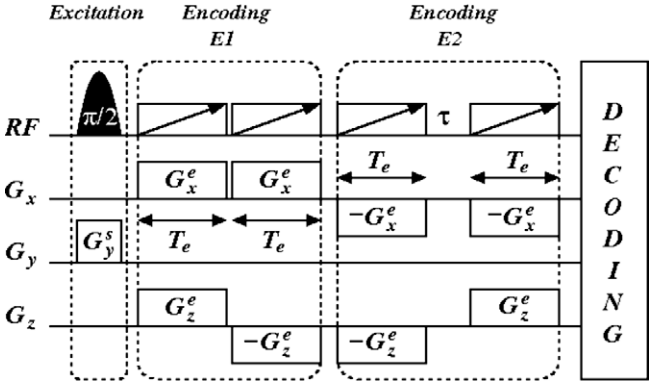

Fig. 2. Cross-encoded scheme designed to compensate for unknown inhomogeneities of the main field. In the second encoding block $E2$, the signs of all gradients are inverted with respect to $E1$. The combined encoding blocks ($E1 + E2$) yield a phase of the transverse magnetization where the effects of all inhomogeneities are cancelled. A delay τ can be inserted between the two adiabatic pulses in $E2$ to attenuate the distortions of the trajectories during the decoding sequence.

all gradients are inverted. If the interval τ = 0 in $E2$, the phase resulting from the encoding unit $E2$ alone is

$$\varphi_{E2}(x,z) = -\lambda_{E2} xz \tag{12}$$

with

$$\lambda_{E2} = 4T_e\gamma^2(G_x^eG_z^e - G_z^e\delta B_0(x,y,z)/x)/\Delta\omega_{ad} \tag{13}$$

Consequently, the effects of inhomogeneous static fields are cancelled by concatenating sequences $E1$ and $E2$:

$$\varphi_e = -2\lambda xz \tag{14}$$

where λ is defined in Eq. (3).

We now focus our attention on the decoding sequence. If we combine the encoding schemes $E1$ + $E2$ of Fig. 2 with the decoding part $D1$ of Fig. 1A, the spatial variation of the static field $\delta B_0(x, y, z)$ yields an additional contribution to the overall phase

$$\Phi(x,y,z,t) = \varphi_e(x,z) + k_x(t)x + k_z(t)z + \gamma\delta B_0(x,y,z)t \tag{15}$$

This phase must again fulfill the conditions of Eq. (7):

$$\begin{aligned} x_k - \frac{\gamma t_k}{2\lambda}\left\{\frac{\partial\,\delta B_0(x,y,z)}{\partial z}\right\}_{(x_k,y_k,z_k)} &= \frac{k_z(t_k)}{2\lambda} \\ z_k - \frac{\gamma t_k}{2\lambda}\left\{\frac{\partial\,\delta B_0(x,y,z)}{\partial x}\right\}_{(x_k,y_k,z_k)} &= \frac{k_x(t_k)}{2\lambda} \end{aligned} \tag{16}$$

The zig-zag trajectory now deviates from the ideal behavior in a homogeneous field because of the terms that are proportional to t_k and to the derivatives of $\delta B_0(x, y, z)$. The signal from the voxel V_k will be affected by static inhomogeneities if the time t_k at which the echo appears is delayed.

During decoding, we can attenuate the effects of static field inhomogeneities but not suppress them completely. A first approximate solution (scheme $D2$ in Fig. 3A) relies on the insertion of a composite pulse $(\pi/2)_y(\pi)_x(\pi/2)_y$ [10] between each pair of decoding gradients as can be done in EPI experiments [11,12]. This leads to an overall phase

$$\Phi(x,y,z,t) = \varphi_e(x,z) + k_x(t)x + k_z(t)z + \gamma\delta B_0(x,y,z)f_{D2}(t) \tag{17}$$

The sign of the term $\gamma\delta B_0(x, y, z)f_{D2}(t)$ is reversed at $t = (2n-1)T_d$ with n = 1, 2, …, N_d. In analogy to $k_z(t)$ in Eqs. (5) and (6), we define:

$$f_{D2}(t) = \int_0^t (-1)^{n_{D2}(t')}dt' \tag{18}$$

where $n_{D2}(t')$ is the integer part of $t'/(2Td)$ + 1/2, resulting in:

$$\begin{aligned} x_k - \frac{\gamma f_{D2}(t_k)}{2\lambda}\left\{\frac{\partial\,\delta B_0(x,y,z)}{\partial z}\right\}_{(x_k,y_k,z_k)} &= \frac{k_z(t_k)}{2\lambda} \\ z_k - \frac{\gamma f_{D2}(t_k)}{2\lambda}\left\{\frac{\partial\,\delta B_0(x,y,z)}{\partial x}\right\}_{(x_k,y_k,z_k)} &= \frac{k_x(t_k)}{2\lambda} \end{aligned} \tag{19}$$

The most severe error in the localization of the voxel of interest V_k occurs when $t_k = (2n\text{-}1)T_{d:}$

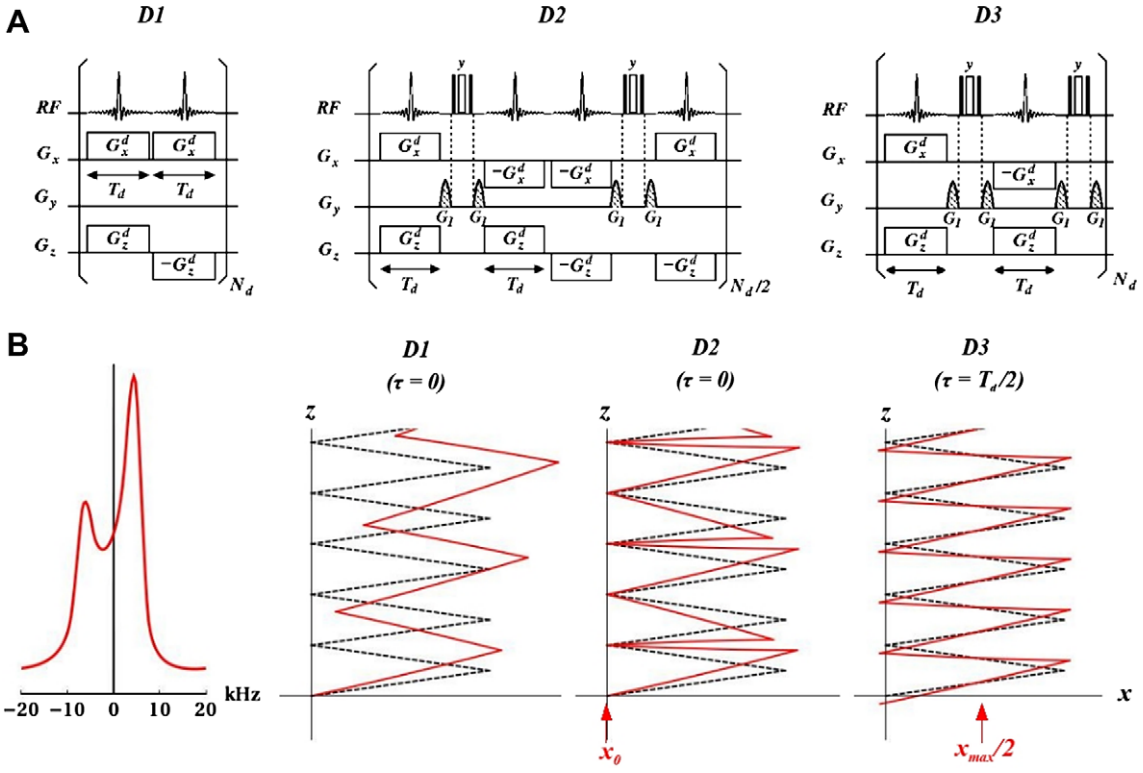

Fig. 3. (A) Comparison of the basic decoding scheme $D1$ of Fig. 1A with two alternative methods $D2$ and $D3$. In scheme $D2$, composite refocusing pulses $90°_x180°_y90°_x$ flanked by two gradients G_1 are inserted between each pair of decoding gradients, while in scheme $D3$ they are inserted after each gradient. (B) Simulated proton spectra and zig-zag trajectories in homogeneous (black dashed lines) and inhomogeneous fields (red continuous lines). The proton spectrum arising from a 4 × 4 × 20 mm sample shows a full-width at half maximum of ~20 kHz. Scheme $D2$ entirely refocuses deviations from the ideal trajectory at $t = 2(n-1)T_d$ with n = 1, 2, …, N_d but leaves errors at $t = (2n-1)T_d$. When a delay $\tau = T_d/2$ is inserted in the encoding sequence $E2$ of Fig. 2, scheme $D3$ results in distorted and ideal trajectories that intersect halfway at $x_{max}/2$ rather than at x_0, and the deviations are reduced by a factor two. (For interpretation of the references to color in this figure legend, the reader is referred to the web version of this paper.)

$$\Delta x_k = \frac{\gamma T_d}{2\lambda}\left\{\frac{\partial \delta B_0(x,y,z)}{\partial z}\right\}_{(x_k,y_k,z_k)}$$
$$\Delta z_k = \frac{\gamma T_d}{2\lambda}\left\{\frac{\partial \delta B_0(x,y,z)}{\partial x}\right\}_{(x_k,y_k,z_k)} \quad (20)$$

In the alternative scheme $D3$ in Fig. 3A, a composite pulse $(\pi/2)_y(\pi)_x(\pi/2)_y$ is inserted after each decoding gradient, and a delay $\tau = T_d/2$ is used in $E2$ (see Fig. 2). The overall phase becomes

$$\Phi(x,y,z,t) = \varphi_e(x,z) + k_x(t)x + k_z(t)z + \gamma\delta B_0(x,y,z) f_{D3}(t) - \gamma\delta B_0(x,y,z)\frac{T_d}{2} \quad (21)$$

where

$$f_{D3}(t) = \int_0^t (-1)^{n_{D3}(t')} dt' \quad (22)$$

with $n_{D3}(t') = n_{D1}(t')$ so that

$$x_k - \frac{\gamma(f_{D3}(t_k) - T_d/2)}{2\lambda}\left\{\frac{\partial \delta B_0(x,y,z)}{\partial z}\right\}_{(x_k,y_k,z_k)} = \frac{k_z(t_k)}{2\lambda}$$
$$z_k - \frac{\gamma(f_{D3}(t_k) - T_d/2)}{2\lambda}\left\{\frac{\partial \delta B_0(x,y,z)}{\partial x}\right\}_{(x_k,y_k,z_k)} = \frac{k_x(t_k)}{2\lambda} \quad (23)$$

The error in the localization of the voxel V_k is halved compared to Eq. (20). This error reaches a maximum at intervals $t_k = T_d$.

In Fig. 3B, we simulate the zig-zag trajectories for the three schemes $D1$, $D2$ and $D3$, describing the intrinsic (time-independent) inhomogeneity of the static field by second-order polynomials:

$$\delta B_0(x,y,z) = (G_x x + F_{xx}x^2, G_y y + F_{yy}y^2, G_z z + F_{zz}z^2) \quad (24)$$

If $G_x = G_y = G_z = 0.001$ T/m and $F_{xx} = F_{yy} = F_{zz} = 0.02$ T/m^2, the breadth of the simulated spectrum of Fig. 3B is around 20 kHz. This leads to a zig-zag trajectory that deviates from the ideal path during the $D1$ decoding sequence. The $D2$ scheme allows one to refocus these deviations at $t = 2(n\text{-}1)T_d$ with $n = 1, 2, \ldots, N_d$ (corresponding to the origin of the x axis), leaving significant deviations near x_{max}. With the $D3$ scheme combined with a delay $\tau = T_d/2$, the distorted and ideal trajectories intersect halfway at $x_{max}/2$ rather than at x_0, and the errors are attenuated by a factor 2.

2.3. Resolution of CE-MRI in homogeneous fields

As for spatial encoding using chirped pulses [5], the resolution of CE-MRI depends only on the encoding conditions. In Fig. 4, we present numerical simulations of the image of square and rectangular two-dimensional objects obtained with the pulse scheme of Fig. 1A. In Fig. 4A–C, the overall phase Φ of Eq. (8) was weighted by factors 0.1, 1 and 10, respectively. This allows one to scale the encoding parameter λ while keeping the same field of view (FOV). The three two-dimensional images and central cross-sections through the square object at $x = 0$ or $z = 0$ illustrate how the resolution depends on λ. The resolution can be improved by increasing the strength and/or length of the encoding gradients. The decoding gradients affect only the FOV but have no influence on the resolution.

By comparing the images of the rectangular 2×30 mm object in Fig. 1C and the square 2×2 mm object in Fig. 4B, one observes a difference in resolution, although the encoding parameters were similar. Clearly, the resolution depends on the dimensions of the object. In Figs. 4D–F, we show that the elongation of the object

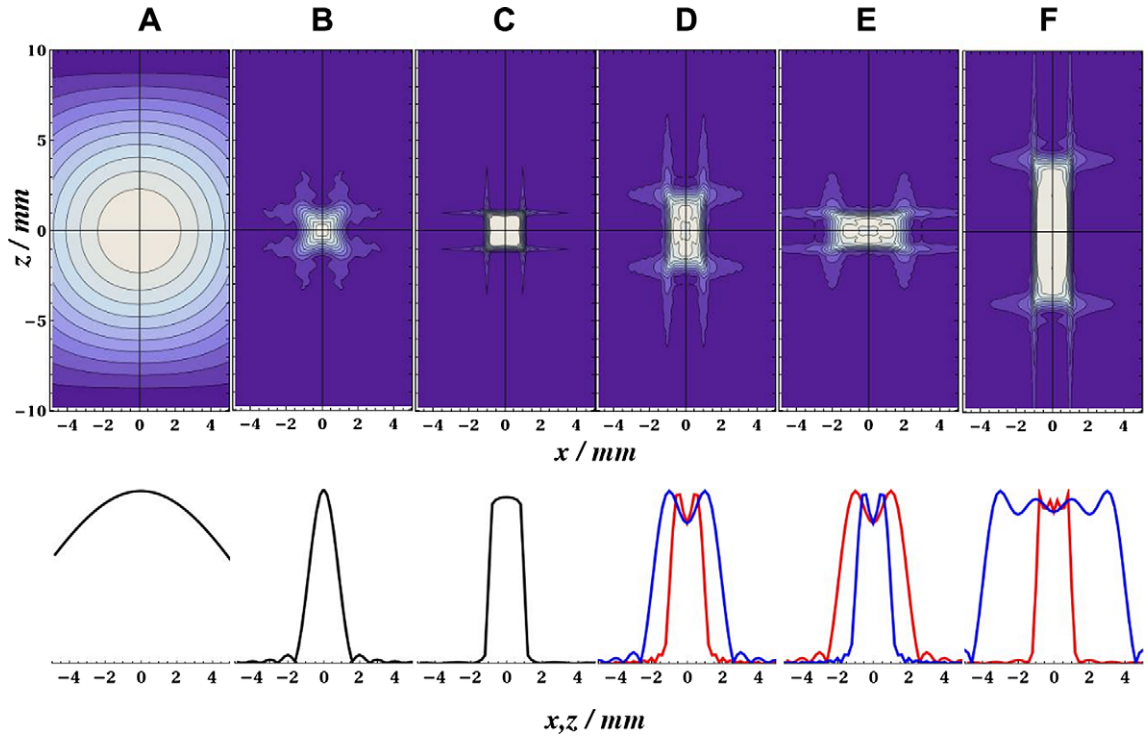

Fig. 4. Effect of encoding parameters and dimensions of the object on the resolution. As in Fig. 1C, numerical simulations of the images of square and rectangular two-dimensional objects were obtained with the pulse scheme of Fig. 1A. The absolute value of the integral of Eq. (4) was calculated at intervals $\Delta x = x_{max}/50$ and $\Delta z = z_{max}/100$ with the following parameters: $G_x^e = G_z^e = 0.022$ T/m, $G_x^d = 0.0241$ T/m and $G_z^d = 0.3864$ T/m, $T_e = 6$ ms, $T_d = 320$ μs, $\Delta\omega_{ad}/(2\pi) = 40$ kHz, $N_d = 16$, resulting in $x_{max} = 10$ mm and $z_{max} = 20$ mm (FOV = 10×20 mm). From A to C, the overall phase Φ of Eq. (8) was weighted by factors 0.1, 1 and 10, respectively. The 2D images and central cross-sections (blue lines for vertical cross-sections at $x = 0$, red lines for horizontal cross-sections at $z = 0$) of a 2×2 mm square object illustrate the dependence of the resolution on the encoding parameter. Elongation of the object along the z axis to 2×4 mm (D) or 2×8 mm (F) or along the x axis to 4×2 mm (E) increases the resolution in the perpendicular direction. (For interpretation of the references to color in this figure legend, the reader is referred to the web version of this paper.)

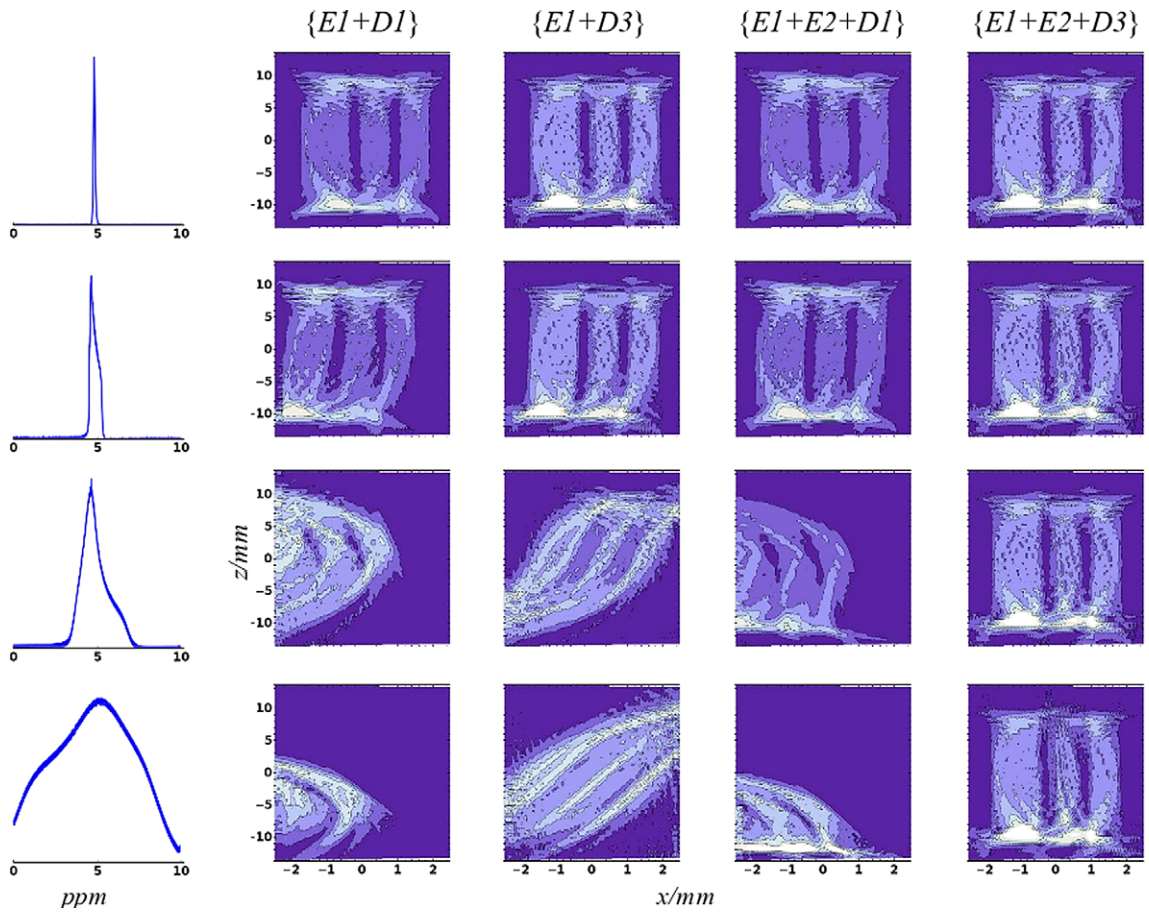

Fig. 5. Comparison of experimental images of a phantom with various combinations of encoding and decoding schemes for an increasingly inhomogeneous static field $\delta B_0(x, y, z)$, characterized by the lineshapes of the water resonance in the absence of any pulsed field gradients (left). A glass capillary (0.9 and 1.6 mm inner and outer diameters) was inserted into a tube with a 3.8 mm inner diameter; the spaces inside the capillary and between the two tubes being filled with water. The experimental conditions were $G_x^e = 0.022$ T/m (for $E1$) or $G_x^e = 0.011$ T/m (for $E1 + E2$), $G_z^e = 0.022$ T/m, $G_x^d = 0.0165$ T/m, $G_z^d = 0.1925$ T/m, T_e = 6 ms, T_d = 320 μs, $\Delta\omega_{ad}/(2\pi) = 40$ kHz, N_d = 32. All experiments were performed with a Bruker Avance 600 MHz (14T) spectrometer equipped with a triple-gradient TBI probe.

in one dimension increases the resolution in the perpendicular direction. In Fig. 4D and E, the object is elongated either along the z axis (2×4 mm) or along the x axis (4×2 mm). This leads to an improvement of the resolution in the x and z dimensions respectively. The figures also illustrate that the dimensions of the FOV have no impact on the resolution. A comparison of the cross-sections in Fig. 4B, D and F (the latter with a 2×8 mm object) highlights a gain in resolution (sharper transitions near the edges) in the x dimension (red lines) while the resolution in the z dimension (blue lines) remains the same (same slope in transition regions).

3. Experimental results

Fig. 5 shows experimental images obtained with a phantom consisting of a glass capillary (0.9 and 1.6 mm for the inner and outer diameters) inserted in a sample tube (3.8 mm inner diameter), where the spaces are filled with water. Various combinations of encoding and decoding schemes were tested from left to right, for increasing static field inhomogeneities $\delta B_0(x, y, z)$ from top to bottom, characterized by the lineshapes of the water resonance recorded in the absence of any pulsed field gradients (left margin). The images are increasingly distorted from top to bottom. Used in isolation, the encoding $\{E1 + E2\}$ schemes or the decoding $D3$ sequence cannot cope with very large inhomogeneities. Only the combination $\{E1 + E2 + D3\}$ gives nearly undistorted images in the most inhomogeneous fields. The combination $\{E1 + E2 + D2\}$ (not shown) gives slightly larger distortions.

Fig. 6 (top half) shows applications of the combined scheme $\{E1 + E2 + D3\}$ to the same phantom as used in Fig. 5 and (bottom half) to a different phantom consisting of a glass spiral inserted in a sample tube (3.8 mm inner diameter). This demonstrates how the new method yields 3D images that are virtually indistinguishable when recorded under dramatically different conditions, regardless whether the homogeneity is good or severely perturbed. The geometrical characteristics of the two phantoms can be determined quite accurately even when the inhomogeneity of the static field leads to a water resonance with a breadth of about 3000 Hz.

4. Conclusions

The novel cross-encoded MRI schemes, using adiabatic pulses and alternating gradients in two perpendicular dimensions, can remove undesirable effects of inhomogeneous magnetic fields that may result from susceptibility effects and prevent blurring due to slow motion since the images are recorded in a fraction of a second. The zig-zag trajectories in the decoding period can be improved by using refocusing pulses. Magnetic resonance images have been recorded in two and three dimensions that are virtually indistinguishable in spite of dramatically different static field inhomogeneities.

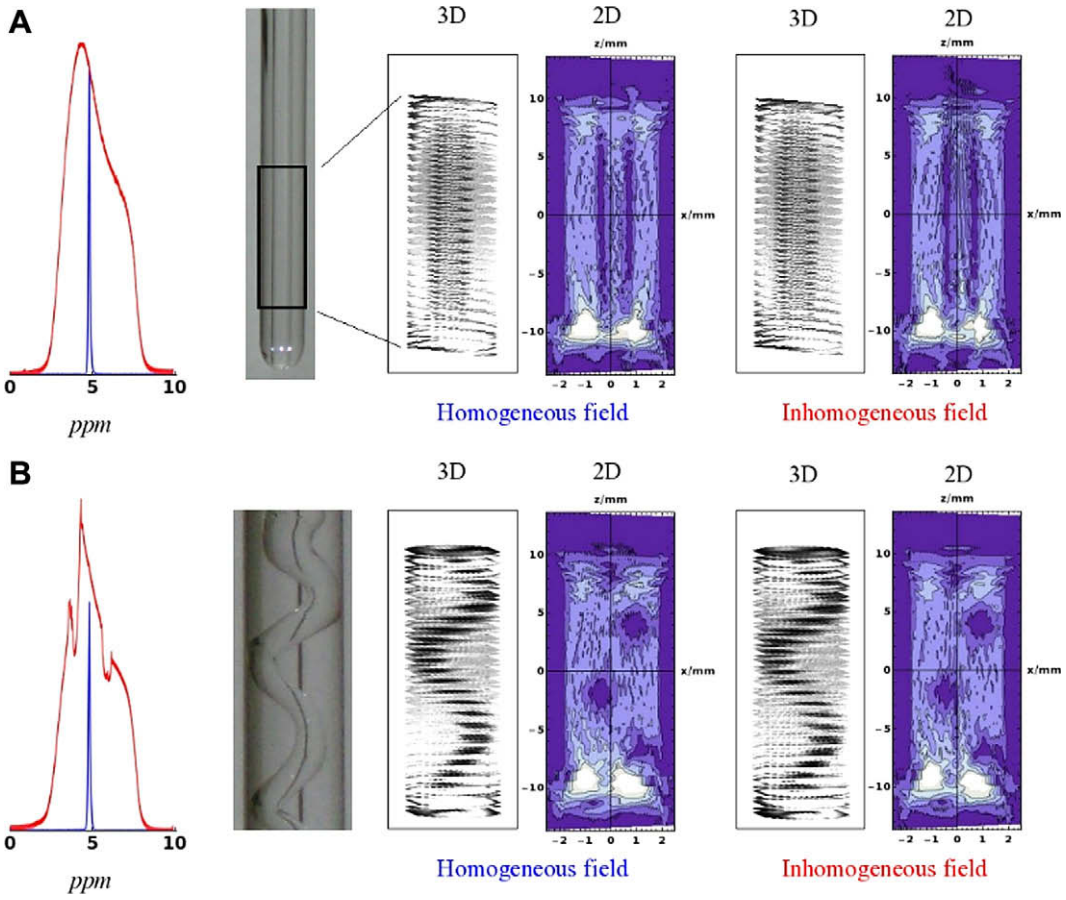

Fig. 6. Images obtained with the combined scheme {*E*1 + *E*2 + *D*3} of Figs. 2 and 3 with (A) the same glass capillary phantom as in Fig. 5, and (B) with a glass spiral phantom surrounded by water inserted into a tube with 3.8 mm inner diameter. Both phantoms were immersed either in homogeneous or inhomogeneous fields characterized by the proton spectra on the left (blue or red lines, respectively). In the *y*-dimension, 32 neighboring slices were recorded with a recovery delay of 10 s between scans. Photographs of the phantoms (black-and-white) are compared with full 3D images obtained by addition of the 32 planes (grey scale) and with 2D images of the central slices (blue scale). In order to visualize the cross-sections of the phantoms, the different planes of the 3D images are stacked following the experimental zig-zag pattern, like the fold of an accordion. The experimental conditions were like in Fig. 5: $G_x^e = 0.011$ T/m, $G_z^e = 0.022$ T/m, $G_x^d = 0.0165$ T/m, $G_z^d = 0.1925$ T/m, T_e = 6 ms, T_d = 320 μs, $\Delta\omega_{ad}/(2\pi) = 40$ kHz, N_d = 32, $\tau = T_d/2$. A Bruker Avance 600 MHz (14T) spectrometer equipped with a triple-gradient TBI probe was used. (For interpretation of the references to color in this figure legend, the reader is referred to the web version of this paper.)

Acknowledgments

We thank Laetitia Zuccarelli for manufacturing the helical glass phantom. This work was supported by the European Union (Integrated Infrastucture Initiative, Contract No. RII3-026145, Joint Research Activity JRA1, Contract No. 026145), the Centre National de la Recherche Scientifique (CNRS, France), the Agence Nationale pour la Recherche (ANR, France), the Fonds National de la Recherche Scientifique (FNRS, Switzerland, No. 200020_124694/1) and the Commission pour la Technologie et l'Innovation (CTI, Switzerland, No. 9991.1 PFIW-IW).

References

[1] P.C. Lauterbur, Image formation by induced local interactions: examples employing nuclear magnetic resonance, Nature 242 (1973) 190–191.
[2] S. Ogawa, T.M. Lee, A.S. Nayak, P. Glynn, Oxygenation-sensitive contrast in magnetic resonance image of rodent brain at high magnetic fields, Magn. Reson. Med. 14 (1990) 68–78.
[3] K.K. Kwong et al., Dynamic magnetic resonance imaging of human brain activity during primary sensory stimulation, Proc. Natl. Acad. Sci. USA 89 (1992) 5675–5679.
[4] M. Stehling, R. Turner, P. Mansfield, Echo-planar imaging: magnetic resonance imaging in a fraction of a second, Science 254 (1991) 43–50.
[5] L. Frydman, T. Scherf, A. Lupulescu, The acquisition of multidimensional NMR spectra within a single scan, Proc. Natl. Acad. Sci. USA 99 (2002) 15858–15862.
[6] Y. Shrot, L. Frydman, Spatially encoded NMR and the acquisition of 2D magnetic resonance images within a single scan, J. Magn. Reson. 172 (2005) 179–190.
[7] A. Kumar, D. Welti, R.R. Ernst, NMR Fourier Zeugmatography, J. Magn. Reson. 18 (1975) 69–83.
[8] A. Tal, L. Frydman, Spatial encoding and the single-scan acquisition of high definition MR images in inhomogeneous fields, J. Magn. Reson. 182 (2006) 179–194.
[9] P. Pelupessy, Adiabatic single scan two-dimensional NMR spectroscopy, J. Am. Chem. Soc. 125 (2003) 12345–12350.
[10] M.H. Levitt, Composite pulses, Prog. Nucl. Magn. Reson. Spectrosc. 18 (1986) 61–122.
[11] D.N. Guilfoyle, P. Mansfield, K.J. Packer, Fluid flow measurement in porous media by echo-planar imaging, J. Magn. Reson. 97 (1992) 342–358.
[12] B. Manz, P.S. Chow, L.F. Gladden, Echo-planar imaging of porous media with spatial resolution below 100 μm, J. Magn. Reson. 136 (1999) 226–230.